An optimized single-crystal to polycrystal model of the neutron transmission of textured polycrystalline materials

Florencia Malamud,[a,b,c]* Javier Roberto Santisteban,[b,c] Miguel Angel Vicente Alvarez,[b,c] Matteo Busi,[a] Efthymios Polatidis[a] and Markus Strobl[a]

[a]Laboratory for Neutron Scattering and Imaging, Paul Scherrer Institut, Forschungsstrasse 111, Villigen PSI, Switzerland, [b]National Scientific and Technical Research Council (CONICET), Argentina, and [c]Laboratorio Argentino de Haces de Neutrones (LAHN), Centro Atómico Bariloche, Avenida Bustillo 9500, San Carlos de Bariloche, Rio Negro 8400, Argentina. *Correspondence e-mail: florencia.malamud@psi.ch

The attenuation coefficient of textured materials presents a complex dependence on the preferred orientation with respect to the neutron beam. Presented here is an attenuation coefficient model to describe textured polycrystalline materials, based on a single-crystal to polycrystalline approach, aiming towards use in full-pattern least-squares refinements of wavelength-resolved transmission experiments. The model evaluates the Bragg contribution to the attenuation coefficient of polycrystalline materials as a combination of the Bragg-reflected component of a discrete number of imperfect single crystals with different orientations, weighted by the volume fraction of the corresponding component in the orientation distribution function. The proposed methodology is designed to optimize the number of single-crystal orientations involved in the calculation, considering the instrument resolution and the statistical uncertainty of the experimental transmission spectra. The optimization of the model is demonstrated through its application to experiments on calibration samples presenting random crystallographic textures, measured on two imaging instruments with different resolutions. The capability of the model to simulate textured samples in different orientations is shown with a copper sample used as a reference in texture studies of archaeological objects and a 316L stainless steel sample produced by laser powder-bed fusion. The ability of the model to predict the attenuation coefficient of polycrystalline textured materials on the basis of a reduced number of texture components opens the possibility of including it in a least-squares fitting routine to perform crystallographic texture analysis from wavelength-resolved transmission experiments.

1. Introduction

Wavelength-resolved neutron imaging has been used to analyse crystallographic texture in various materials (Lehmann *et al.*, 2009, 2014; Santisteban, Edwards & Stelmukh, 2006; Sato *et al.*, 2011; Shiota *et al.*, 2017). The analysis is based on the sensitivity of the wavelength-dependent neutron transmission signal of a polycrystalline material with respect to the crystallographic texture of the sample and the orientation of the specimen in the neutron beam. For samples with uniform texture along the neutron beam direction, it is possible to simulate the neutron transmission spectrum when the orientation distribution function (ODF) of the specimen is already known, and different approaches have been employed over the years. Santisteban, Edwards & Stelmukh (2006) extended the neutron elastic coherent cross-section expression obtained by Fermi *et al.* (1947) for random crystallographic textured polycrystalline materials to textured
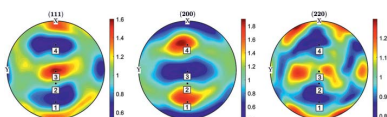
samples. They introduced a correction factor, which accounts for the difference in the diffracting volume fraction of a textured specimen compared with a material with random crystallographic texture. This approach has been applied to a combination of simple models for the ODF [such as individual components (Malamud & Santisteban, 2016; Santisteban *et al.*, 2012) or fibre texture components (Vogel, 2000)] and it has been used to study several materials (Malamud *et al.*, 2014; Santisteban *et al.*, 2012). In a recent paper, Laliena *et al.* (2020) derived a compact expression for the elastic coherent cross section for textured materials by analytical integration of the expression proposed by Santisteban, Edwards & Stelmukh (2006) when the ODF is expressed in terms of its Fourier components. The coherent elastic cross-section term is reduced to a summation of functions weighted by the Fourier coefficients of the ODF.

Dessieux *et al.* (2018) presented a very different methodology, considering the transmission contribution of each single-crystal grain to generate the total neutron cross section of a polycrystalline textured material. The model calculates the neutron transmission for each crystallite grain as a function of neutron wavelength, crystal structure and crystal orientation, including the crystal mosaicity and its orientation in the neutron beam as input parameters, employing a Gaussian instrumental function to convolve the simulated intensity. This approach has been applied to simulate the effect of deformation and recrystallization textures of an additively manufactured Inconel 718 specimen (Dessieux *et al.*, 2019).

Although it is not currently possible to quantify a completely unknown ODF from a neutron imaging experiment, different models have been implemented in order to extract crystallographic texture information for a material from transmission experiments. The first approaches involved the introduction of the March–Dollase formulation for fibre textures in a Rietveld refinement analysis of transmission data (Vogel, 2000; Sato, 2017; Sato *et al.*, 2010). As an anisotropy factor, this quantity measures the degree of departure of the experimental data from those expected for a sample with random crystallographic texture, and it has been used to study *e.g.* Al welds (Sato *et al.*, 2011; Kardjilov *et al.*, 2012). A different approach involves using the height of the Bragg edges to quantify the fraction of crystals with their plane normal to the neutron beam direction (Malamud, 2016; Busi *et al.*, 2021). This method does not take into account the shape of the transmission spectrum for wavelengths in between the Bragg edges, which is also strongly dependent on the crystallographic texture. From the Fourier expansion of the elastic coherent cross section, Vicente Alvarez *et al.* (2021) developed a method to estimate the integral parameters of the ODF (such as Kearns factors in hexagonal crystals) and tensorial properties of textured polycrystals from wavelength-resolved neutron transmission experiments.

Here, we present a different version of the single-crystal to polycrystalline model introduced by Dessieux *et al.* (2018), aimed towards its use in full-pattern least-squares refinements of wavelength-resolved transmission experiments. For this purpose, we propose a methodology designed to optimize the number of single-crystal orientations involved in the calculation with the actual resolution of the instrument and the statistical uncertainty of the experiment. The present methodology is based on equations developed to describe and fit the full-pattern transmission spectra of mosaic crystals (Malamud & Santisteban, 2016) and oligo-crystalline materials (Malamud *et al.*, 2022). The reduced number of crystal orientations required to describe the ODF in the present approach enables its introduction in a least-squares fitting routine to refine the volume fractions of the selected components, unlocking the possibility of employing wavelength-resolved neutron imaging experiments to perform quantitative crystallographic texture analysis of polycrystalline materials. This paper is organized as follows. Section 2 gives a description of neutron transmission experiments on textured polycrystalline materials and mosaic crystals, and Section 3 presents the theoretical expressions required to describe the transmission of textured specimens. A full description of the Bragg-reflected contribution of a mosaic crystal adopted in this work is provided by Malamud & Santisteban (2016), and a detailed description of the profile function and the parameterization of the peak width is presented in Appendix *A*. Section 4 establishes the assumptions and expressions of our improved single-crystal-based model, together with the methodology for optimizing its basic input parameters, and Section 5 provides details about the practical implementation of the equations within a computing system. Section 6 describes the studied samples and the optimized model parameters. Section 7 demonstrates the capability of the model through its application to experiments on calibration samples presenting random crystallographic textures and on textured materials measured along different directions: a copper sample used as a reference in texture studies of archaeological objects (Artioli, 2007) measured on ENGIN-X at the Rutherford Appleton Laboratory (UK), and a 316L stainless steel sample produced by laser powder-bed fusion measured on RADEN at J-PARC Laboratory (Japan) (Busi *et al.*, 2022). Finally, the expected capabilities and limitations of the model introduced here are discussed in Section 8.

2. Neutron transmission of textured crystalline materials

In a neutron transmission experiment, a polychromatic collimated neutron beam is incident on a specimen [Fig. 1(*a*)], and the transmission $T(\lambda)$ is determined by normalizing the signal recorded by a detector when the sample is in the beam, $I(\lambda)$, with the incident beam recorded without the specimen, $I_0(\lambda)$,

$$T(\lambda) = \frac{I(\lambda)}{I_0(\lambda)}. \qquad (1)$$

Since neutrons with different wavelengths are diffracted differently by a crystalline material, depending on the crystal structure and its microstructure and texture, the wavelength-resolved transmission signal can provide valuable information to characterize these quantities. Fig. 1(*b*) shows the fraction of
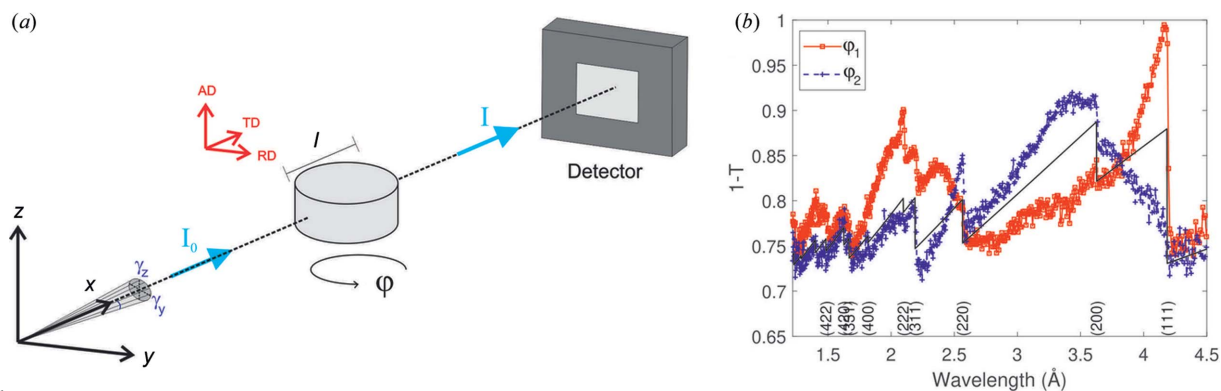
Figure 1
(*a*) A schematic representation of a neutron transmission experiment. (*b*) Spectra of the fraction of neutrons removed by a textured copper sample from the incident beam along two different directions (red and blue symbols), compared with the spectrum expected for a specimen with random crystallographic texture (solid black line).

neutrons removed from the beam, as given by $1 - T(\lambda)$, by a textured 1 cm thick copper specimen along two different directions, obtained by rotating the specimen around the vertical direction. The spectra are characterized by the presence of Bragg edges, appearing at wavelengths corresponding to twice the interplanar distances of the different crystal planes. As seen in the figure, the edge heights change greatly for the different orientations, whilst the regions between the Bragg edges are continuous functions of wavelength.

A textured material is defined as a fine-grained polycrystalline material where the component crystallites are preferentially present in particular orientations or have some crystal directions aligned to specific directions of the specimen (*e.g.* axial, radial, transverse). This non-uniform distribution of orientations can be described by a probability density function, usually referred to as the orientation distribution function (Kocks, 2000). The ODF gives the number of crystallites present in a sample for each possible crystallite orientation. The changes observed in the Bragg edge spectra arise because different numbers of crystal planes fulfil the diffraction condition for the different orientations of the specimen. For comparison, Fig. 1 includes the spectrum $R_{\mathrm{random}}(\lambda)$ expected for a specimen of similar thickness but composed of an aggregate of small (1–10 µm) crystallites with random crystallographic orientations (Fermi *et al.*, 1947). We observe that such a model is not capable of describing the measured spectra of textured samples, so a different, more complex, model is indeed necessary.

The goal of this work is to evaluate efficiently the spectra observed in Fig. 1(*b*) as the sum of the individual diffracting signals from different crystallite groups, separated according to their orientation. Each crystalline group will be described by its mean orientation and a characteristic misalignment around that orientation. In this sense, these groups share a similarity with a mosaic crystal, *e.g.* a single crystal having a certain 'mosaic' substructure that produces small angular deviations around the average orientation of the crystal, usually expressed in terms of a mosaicity η, representing the width of a Gaussian distribution of misorientations

(Schneider, 1974). Fig. 2 shows the fraction of neutrons removed from the incident neutron beam by a 1 cm thick mosaic copper crystal. In contrast to Fig. 1, the spectrum is composed of a series of peaks appearing at specific neutron wavelengths, due to diffraction by those crystallographic planes that fulfil Bragg's law (Santisteban, 2005). These peaks are similar to the spots observed in traditional Laue diffraction experiments. The position, height and width of these Laue peaks depend on the material properties, the orientation and mosaicity of the crystal, and the resolution of the instrument (Malamud & Santisteban, 2016). The Laue peaks appear on top of a rather smooth background, due to the combined effects of nuclear absorption $A(\lambda)$ and thermal diffuse scattering $S(\lambda)$, which are nearly identical for both mosaic crystals and polycrystalline specimens.

The model proposed here will construct the spectra observed in Fig. 1(*b*) as a weighted sum of a large number of spectra similar to the one presented in Fig. 2. The model assumes that the ODF of the polycrystalline material can be considered as being composed of a set of radially symmetric
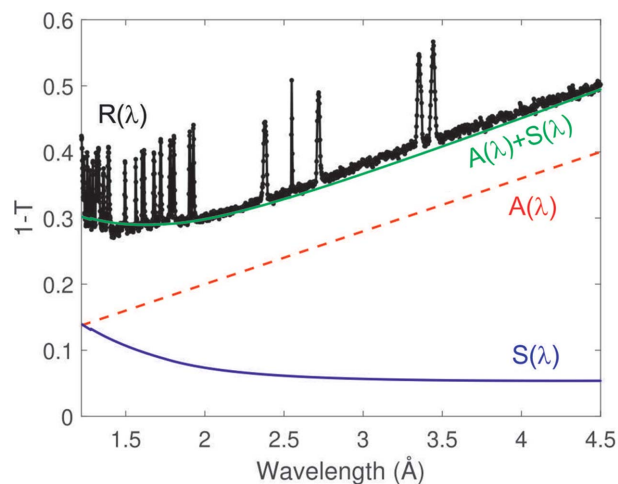

Figure 2
The fraction of neutrons removed by a copper mosaic specimen from a neutron beam incident along the [110] direction.

functions in the orientation space, known as unimodal components. The Bragg contribution to the attenuation coefficient is calculated as a summation of the individual attenuation contributions weighted by their volume fractions. To do this, the orientation space is discretized in a series of orientations depending on the resolution function of the neutron instrument, and with a width dictated by the statistical uncertainty of the measurement.

3. Transmission spectra and ODF

Within the kinematic theory of diffraction, the probability of a neutron being removed from the transmitted beam is proportional to an attenuation coefficient $\mu(\lambda)$,

$$1 - T(\lambda) = 1 - \exp\left[-\mu(\lambda)\, l\right], \tag{2}$$

where l is the thickness of the specimen along the neutron beam direction. $\mu(\lambda)$ can be defined according to the different processes contributing to the attenuation coefficient,

$$\mu(\lambda) = \mu_A(\lambda) + \mu_S(\lambda) + \mu_R(\lambda), \tag{3}$$

where the subscripts A, S and R refer to absorption, scattering and Bragg reflection, respectively. As described above, both absorption and scattering contributions display a smooth dependence on the neutron wavelength. The absorption contribution in the relevant wavelength range is given by a linear dependence on λ as

$$\mu_A(\lambda) = \sigma_{\text{abs}}\left(\frac{\lambda}{\lambda_0}\right), \tag{4}$$

where σ_{abs} is the microscopic absorption cross section of the unit cell at a specific wavelength λ_0. The scattering contribution $\mu_S(\lambda)$ includes a combination of incoherent scattering and inelastic scattering. It can be evaluated using the theoretical expressions given by Granada (1984), depending on the mass A contained in the crystal unit cell, the Debye temperature Θ_D, and the coherent and incoherent cross sections of the scattering, σ_{coh} and σ_{inc}, respectively. The explicit implementation of $\mu_S(\lambda)$ employed in this work can be found in the appendix of the report by Malamud & Santisteban (2016).

The Bragg contribution to the attenuation coefficient depends on the crystal structure and microstructure of the specimen, as well as on the orientation of the sample in the neutron beam $\mathbf{y}$. This contribution can be written as a function of the elastic coherent neutron cross section $\sigma_{\text{coh}}^{\text{ela}}(\lambda)$ as

$$\mu_R(\lambda, \mathbf{y}) = n\, y_{\text{ext}}\, \sigma_{\text{coh}}^{\text{ela}}(\lambda, \mathbf{y}), \tag{5}$$

where y_{ext} represents the extinction factor. $\sigma_{\text{coh}}^{\text{ela}}(\lambda, \mathbf{y})$ is strongly dependent on the crystallographic texture of the sample, described by the ODF (Kocks, 2000). The ODF gives the number of crystallites present in the sample for each possible crystallite orientation g, represented for instance by three Euler angles $(\varphi_1^C, \Phi^C, \varphi_2^C)$ in the coordinate system of the specimen.

More strictly, the ODF $f(g)$ corresponds to the probability density associated with each orientation g, e.g. the volume fraction of crystals that are in that specific orientation,

$$f(g) = \frac{1}{V}\frac{\mathrm{d}V(g)}{\mathrm{d}g}, \quad \text{where } \int_{\text{FZ}} f(g)\,\mathrm{d}g = 1, \tag{6}$$

and $f(g)$ needs only to be defined in the fundamental zone (FZ) of the orientation space SO(3).

The explicit dependence of $\sigma_{\text{coh}}^{\text{ela}}$ on the ODF can be written as (Laliena et al., 2020)

$$\sigma_{\text{coh}}^{\text{ela}} = \frac{n(2\pi)^3}{vk^3}\sum_{hkl}\left|F_{G_{hkl}}\right|^2 \int \mathrm{d}g\, f(g)\, k\, \delta\left(\left|k\hat{z} - gG_{hkl}\hat{z}\right| - k\right), \tag{7}$$

where v is the volume of the unit cell, $\mathbf{k}$ is the wavevector of the incident neutrons, $\mathbf{G}_{hkl}$ is a reciprocal-lattice vector attached to the fixed crystal frame and $\left|F_{G_{hkl}}\right|^2$ is the corresponding structure factor.

For a perfectly isotropic polycrystalline specimen, the coherent elastic cross section does not depend on the orientation of the specimen in the neutron beam. It is computed by considering all the crystallites contributing to a Debye–Scherrer cone (Fermi et al., 1947), obtaining

$$\sigma_{\text{coh}}^{\text{ela}}(\lambda) = \frac{n\lambda^2}{4v}\sum_{hkl}\left|F_{G_{hkl}}\right|^2 d_{hkl}. \tag{8}$$

4. Proposed model

Many models exist to evaluate the ODF of a textured material. Here the ODF will be represented by the superposition of radially symmetric kernel functions ψ centred at each crystallographic orientation g ($g_i = 1, \ldots, N$) on top of a uniform function [$f_{\text{random}}(g) = 1 \,\forall\, g \in \text{FZ}$] (Hielscher, 2013),

$$f(g) = \left(1 - \sum_{i=1}^N w_i\right)f_{\text{random}}(g) + \sum_{i=1}^N w_i\,\psi\left[\angle(g_i, g)\right], \tag{9}$$

where $\angle(g_i, g)$ denotes the angle between the orientation g_i and g, and w_i is the weight associated with each kernel function. Mathematically, the kernel functions $\psi: \text{SO}(3) \rightarrow \mathbb{R}$ only depend on the distance from g to the centre of rotation g_i, and in texture analysis they appear as unimodal bell-shaped model ODFs with a characteristic width dg. In this way, the texture is described as a superposition of unimodal components defined by the selected kernel function ψ. This representation is implemented in the texture analysis software MTEX to estimate the ODF from pole figures measured in diffraction or from the orientations identified in electron backscatter diffraction images (Hielscher & Schaeben, 2008; Hielscher, 2013). The ODF estimator is defined as the solution of a minimization problem, where the unknown ODF is approximated by a linear combination of up to 100 000 unimodal bell-shaped standard ODFs, and the inversion is numerically performed by applying fast Fourier techniques to the rotation group SO(3) and the sphere S2 (Hielscher & Schaeben, 2008).

With this in mind, a textured specimen is described here as composed of a large number of adequately small crystallites, separated into $N + 1$ groups according to their orientation.

N of the groups are angularly very narrow, whilst the remaining group represents a completely random group of orientations within the SO(3) space. In real space, it is assumed that the crystallites have nearly spherical shapes and a size smaller than the primary extinction length (typically 1–40 µm), and the grains composing each group are uniformly distributed across the specimen, separated by a distance larger than the secondary extinction length (Sears, 1997). In this approximation, no extinction effects are considered, and therefore the spectra $R^{\text{tex}}(\lambda)$ of textured materials can be written as a sum of the $R_i(\lambda)$ components of the individual groups, plus a contribution from a polycrystalline material with random crystallographic texture, $R_{\text{random}}(\lambda)$.

Considering the linearity between the elastic coherent cross section and the ODF of equations (7) and (9), the Bragg contribution to the attenuation coefficient of textured materials $\mu_{\text{R}}(\lambda, \mathbf{y})$ can be written as

$$\mu_{\text{R}}(\lambda, \mathbf{y}) = \left(1 - \sum_{i=1}^{N} w_i\right)\mu_{\text{random}}(\lambda) + \sum_{i=1}^{N} w_i \mu_{\psi_i}(\lambda, \mathbf{y}), \quad (10)$$

where $\mu_{\text{random}}(\lambda)$ represents the Bragg contribution of a randomly oriented sample, calculated from equation (8), and $\mu_{\psi_i}(\lambda, \mathbf{y})$ is the attenuation coefficient of the unimodal component ψ centred at g_i,

$$\mu_{\psi_i}(\lambda, \mathbf{y}) = \sum_{hkl} \mu_{\text{R}i}^{hkl} P^{\psi_i}(\lambda_{hkl}, \varpi_{hkl}, \lambda). \quad (11)$$

The function $P(\lambda_{hkl}, \varpi_{hkl}, \lambda)$ describes the actual peak shape depending on the specific instrument (Malamud & Santisteban, 2016). In this expression, we explicitly include the dependence on the beam direction $\mathbf{y}$ in the coordinate system of the sample.

In this work, the ODF of the sample is defined as a superposition of unimodal components using ψ as a de la Valleé Poussin kernel function (Schaeben, 1997), where the half width can be controlled by a single parameter $\beta > 1$. In the present approach, the unimodal component centres g_i are defined by imposing an equi-spaced SO(3) grid on the FZ of the orientation space. The distance Δg_i between adjacent orientations, *i.e.* the resolution of the orientation space, and the β parameter have a profound impact on the ODF representation, and they can be optimized depending on the texture of the sample and the experimental conditions (Biswas *et al.*, 2020).

Here we propose to define the number of unimodal components (N) from the instrumental resolution of the neutron transmission instrument. For a given wavelength resolution $\Delta\lambda/\lambda$, the distance between two adjacent component centres Δg_i is derived from Bragg's law as

$$\frac{\Delta\lambda}{\lambda} = \frac{\lambda_{hkl} - \lambda}{\lambda_{hkl}} = 1 - \cos(\Delta g_i), \quad (12)$$

where $\lambda = 2d_{hkl}\cos g_i$. This gives Δg_i as

$$\Delta g_i = \cos^{-1}\left(1 - \frac{\Delta\lambda}{\lambda}\right). \quad (13)$$

The number N of unimodal components in the FZ is

$$N = \frac{V_{\text{FZ}}}{\Delta g_i}, \quad (14)$$

where V_{FZ} is the volume of the FZ that depends on the crystal and specimen symmetry. In particular, for cubic crystal symmetry and triclinic specimen symmetry, the FZ within the Bunge–Euler orientation space is (Bunge, 1982)

$$\text{FZ} = \begin{cases} (\varphi_1, \Phi, \varphi_2) \,|\, 0 \leq \varphi_1 \leq 2\pi, \\ \cos^{-1}\left[\cos\varphi_2/(1 + \cos^2\varphi_2)^{1/2}\right] \leq \Phi \leq \pi/2, \\ 0 \leq \varphi_2 \leq \pi/4. \end{cases} \quad (15)$$

The half-width β of the kernel function is defined considering the relative statistical uncertainty $\Delta\mu/\mu$ of the measurements, with the requirement of fulfilling the normalization condition of equation (8) for a polycrystalline material with random crystallographic texture. For a given Δg_i resolution, the ODF of a sample with random crystallographic texture $\tilde{f}_\beta(g)$ can be constructed as a superposition of N unimodal components with a half-width β, where the volume fraction of each component is equal to $1/N$.

In the present model, the kernel parameter β is defined by considering that the error between the estimated $\tilde{f}_\beta(g)$ and a uniform ODF $f_{\text{random}}(g)$ should be similar to the statistical uncertainty of the measurements. As an error measure, we consider the $L2$ norm defined as

$$||\tilde{f}_\beta - f_{\text{random}}||_2 = \frac{\int_{\text{SO}(3)} |\tilde{f}_{\text{random}}(g, k) - \tilde{f}_\beta(g)| \, dg}{2 \int_{\text{SO}(3)} |f_{\text{random}}(g)| \, dg}. \quad (16)$$

5. Model implementation

The Bragg attenuation coefficient model has been implemented within the MATLAB programming environment, employing the *MTEX* toolbox (Hielscher & Schaeben, 2008). The code incorporates the equations presented in the previous sections and the sample properties [crystal symmetry, lattice parameter, ODF, absorption, incoherent and coherent microscopic cross sections (σ_{abs}, σ_{inc} and σ_{coh}, respectively), atomic mass A, and Debye temperature Θ_{D}], together with experimental information [$\Delta\lambda/\lambda$, average/representative relative statistical uncertainty of the measurement $\Delta\mu/\mu$, the divergence of the incident neutron beam γ, the instrument decay constant $\tau_{hkl}(\lambda)$ and the orientation of the sample in the
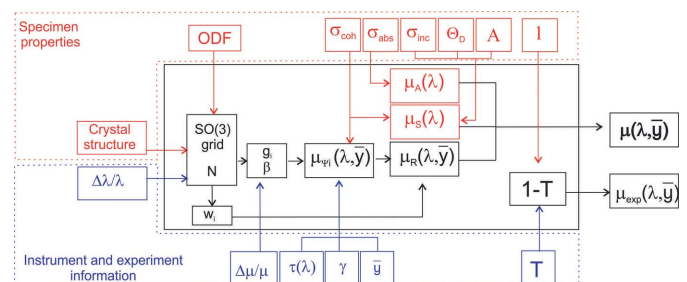

Figure 3
The architecture of the code. See the text for definitions of the symbols.

beam $\mathbf{y}$], to calculate the total linear attenuation coefficient of a polycrystalline material. Fig. 3 displays the code architecture.

For a given $\Delta\lambda/\lambda$ and using the sample crystalline structure, the code generates an equi-spaced grid with the corresponding resolution in the fundamental region, where the ODF is evaluated to extract the volume fractions w_i. For each uni-modal component centred at g_i with half-width β, the model evaluates the neutron attenuation coefficient $\mu_{\psi_i}(\lambda, \mathbf{y})$ [equation (11)] and generates the $\mu_R(\lambda, \mathbf{y})$ weighting each component by their corresponding volume w_i plus a uniform portion. Finally, the code incorporates the absorption [equation (8)] and scattering contributions (Granada, 1984) to produce the total neutron linear attenuation coefficient.

6. Samples and measurements

The capability of the proposed model to calculate the measured neutron attenuation coefficient of specimens with random crystallographic texture and textured materials along different directions of the specimen is demonstrated in the following subsections. The validation is performed by comparing the linear attenuation coefficient with the experimental $\mu(\lambda)$, obtained from the measured transmission signal $T(\lambda)$ using equation (4). The studied samples include a polycrystalline copper sample with random crystallographic texture and an α-iron powder, together with a textured copper specimen and a 316L austenitic stainless steel specimen produced by laser powder-bed fusion (LPBF). The physical properties required to perform the modelling of each sample and to calculate $\mu_A(\lambda)$ and $\mu_S(\lambda)$ are listed in Table 1. For the 316L sample, the atomic mass, scattering length and σ_{abs} were calculated considering the nominal chemical composition of the alloy (Fe–17Cr–12Ni–2.3Si–2.5Mo–0.03C) and using the free atom condition (Granada, 1984).

Figure 4
The $L2$ error between the estimated $\tilde{f}_\beta(g)$ for a specimen with random crystallographic texture and a uniform ODF for different grid resolutions, as a function of the half-width β.

Table 1
Physical parameters of the examined samples.

F.c.c. stands for face-centred cubic and b.c.c. denotes body-centred cubic. The scattering lengths b and neutron cross sections σ_{abs} and σ_{inc} were taken from the list compiled by NIST (*Neutron Scattering Lengths and Cross Sections*, https://www.ncnr.nist.gov/resources/n-lengths/). The Debye temperatures Θ_D were taken from Sears & Shelley (1991). The lattice parameter for 316L steel was taken from Morgano *et al.* (2020).

Sample	Crystal structure	Lattice parameter (Å)	b (fm)	σ_{abs} (barn)	σ_{inc} (barn)	Θ_D (K)	A
Cu	F.c.c.	3.6149	7.718	3.78	0.55	343	63.55
Fe	B.c.c.	2.8665	9.45	2.56	0.4	436	55.847
316L	F.c.c.	3.5964	8.433	2.818	0.55 (Fe)	436 (Fe)	55.918

Table 2
Instrumental resolution $\Delta\lambda/\lambda$, statistical uncertainty on the measurements $\Delta\mu/\mu$, grid resolution Δg_i, the number of components N and the kernel half-width β for different instruments.

Instrument	$\Delta\lambda/\lambda$ (%)	$\Delta\mu/\mu$ (%)	Δg_i (°)	N	Half-width (β, °)
ENGIN-X	0.15	3.25	4	9807	2.3
RADEN	0.25	3	5	4958	3.1
IMAT	0.4	3.25	6	2881	3.7

Wavelength-resolved neutron transmission experiments were performed on ENGIN-X (Santisteban, Daymond *et al.*, 2006) and IMAT (Kockelmann *et al.*, 2013) located at the ISIS Facility, UK, and on RADEN (Shinohara *et al.*, 2020) at the J-PARC pulsed neutron spallation source, Japan. In all cases, the resolution function of the instrument is described by a Gaussian distribution convoluted with a truncated decaying exponential, with a time constant depending on the specific moderator (Kropff *et al.*, 1982). The corresponding wavelength resolutions in the wavelength ranges $\Delta\lambda/\lambda > 0.15$, 0.25 and 0.4% for ENGIN-X, RADEN and IMAT lead to grid resolutions of 4, 5 and 6°, respectively. On the other hand, the statistical uncertainties of the measurements were dependent on the wavelength interval, with typical values of 3.2% for ENGIN-X, 3% for RADEN and 3.2% for IMAT. To define the β parameter for the different experiments, Fig. 4 shows the $L2$ error [equation (16)] between the estimated $\tilde{f}_\beta(g)$ as a function of the half-width β for a specimen with random crystallographic texture and a uniform ODF for different grid resolutions ($\Delta g_i = 4$, 5 and 6°). The figure identifies the corresponding β parameters that match the statistical uncertainty of the measurement according to the $L2$ errors. The corresponding half-widths are 2.3, 3.2 and 3.7° for ENGIN-X, RADEN and IMAT measurements, respectively. Table 2 shows the grid resolution, number of components and kernel half-width for the different $\Delta\lambda/\lambda$ and $\Delta\mu/\mu$ resolutions employed in the simulations. In all cases the quality of the simulation has been quantified by means of the R_p parameter (Jansen *et al.*, 1994), defined as

$$R_p(\%) = 100 \frac{\sum_i |y_i(\text{obs}) - y_i(\text{calc})|}{\sum_i |y_i(\text{obs})|}, \qquad (17)$$
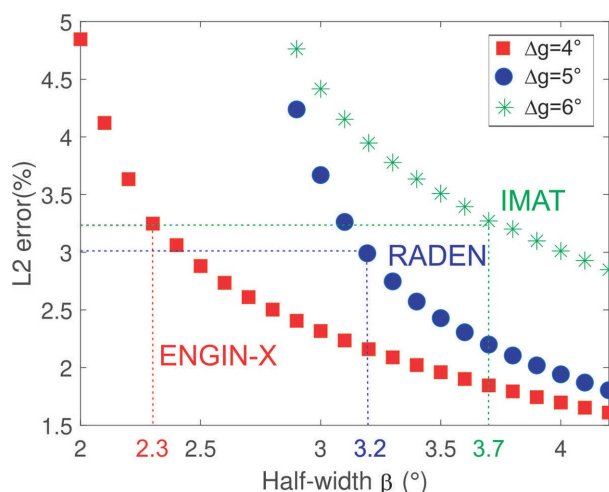
where y_i(obs) and y_i(calc) are the observed and calculated intensities, respectively.

7. Results

7.1. Powder specimens

Fig. 5(a) shows the linear attenuation coefficient of a fine-grained copper powder specimen of $l \simeq 1$ cm measured on ENGIN-X with a neutron beam divergence of 0.3° (red dots), the neutron attenuation coefficient calculated by the proposed model (solid black line), and the residual between the simulation and the experimental data. In this case, the ODF of the powder is described as a superposition of 9807 identically weighted de la Vallée Poussin-shaped kernel functions on an equi-spaced 4° resolution grid in the FZ of cubic symmetry specimens with a 2.3° half-width. As shown in the figure, the model fully describes the height and position of the measured Bragg edges, with an R_p value of 1.75%, demonstrating the capability of the proposed model to describe the attenuation coefficient of polycrystalline specimens with random crystallographic texture.

The effect of the wavelength resolution of the instrument on the experimental attenuation coefficient can be observed in Fig. 5(b), where the Bragg edges corresponding to the (221), (220), (311) and (222) lattice planes of an α-iron powder measured on ENGIN-X (red dots) and IMAT (blue squares) are compared. For the simulation of the ENGIN-X data the same grid as in the previous case was employed, while for the simulation of the attenuation coefficient measured on IMAT the ODF was described using 2881 unimodal components with identical weight on an equi-spaced 6° resolution grid with a 3.7° half-width. The resulting calculated attenuation coefficients for both instruments are shown by solid lines in Fig. 5(b), with resulting R_p values of 2% for the ENGIN-X and 5% for the IMAT measurement. This demonstrates that the model captures the difference in the Bragg edge tails of the

ENGIN-X measurement in comparison with the IMAT data, as highlighted in Fig. 5(b), and the overall effect of the resolution, as can also be appreciated from the difference curve shown at the bottom of Fig. 5(b).

7.2. Textured copper specimen

We analysed a textured copper sample that was produced especially to identify possible manufacturing processes of prehistoric copper axes (Artioli, 2007). The specimen is an irregular parallelepiped of dimensions $\sim 20 \times 20 \times 10$ mm that shows a marked fibre texture due to columnar grain growth during crystallization, as shown in Fig. 6(a). The crystallographic texture of the sample has been used as a standard in a comparison of the performance of different instruments and data collection strategies. In this case, the ODF of the sample was determined by employing neutron diffraction measurements on ENGIN-X and the *NyRTex* texture analysis routine (Malamud *et al.*, 2014). The wavelength-resolved neutron transmission of the sample in different orientations was measured on ENGIN-X, simultaneously with diffraction measurements, using an incident beam divergence of $\sim 0.5°$. The explored neutron beam directions in the sample reference system are labelled from 1 to 4 in the pole figures. Fig. 6(b) shows the corresponding measured attenuation (blue crosses) together with the model. In the calculation, the crystallographic texture of the sample was described by evaluating the volume fractions of the ODF determined by *NyRTex* on an equi-spaced 4° resolution grid using a 2.3° half-width, with no uniform portion. The results of the calculations for the different orientations are shown in Fig. 6(b) as solid red lines, together with the expected attenuation spectrum of a copper sample with random crystallographic texture (dotted black line). In all cases, a very good overall agreement is found between the experimental data and model calculations, with corresponding R_p values of 8.2, 8.12, 10.1 and 11.2% for orientations 1 to 4, respectively.
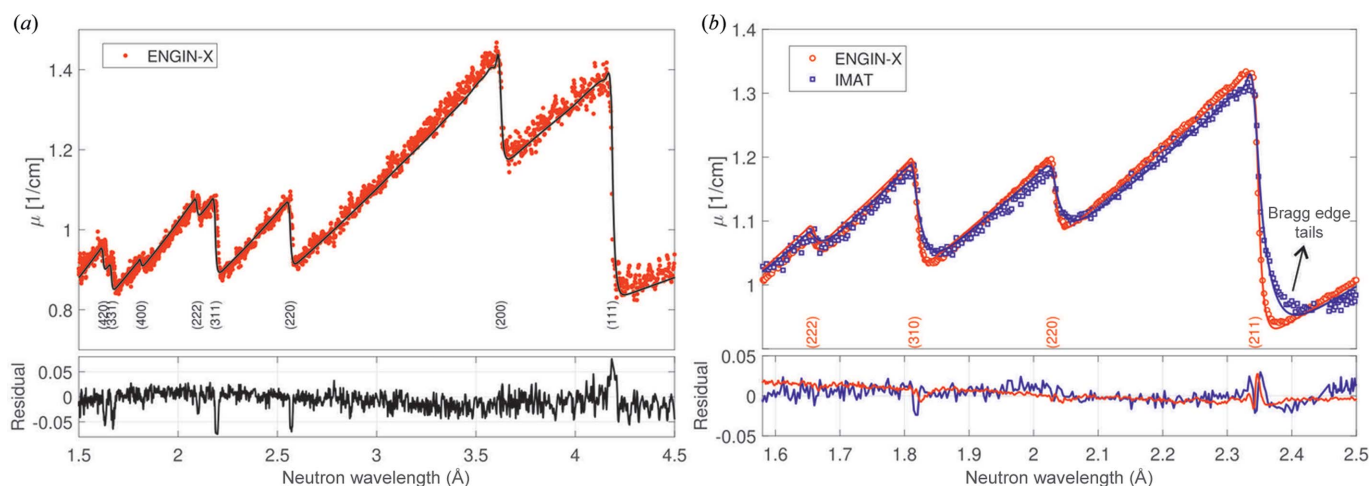

Figure 5
(a) Attenuation coefficient of a copper specimen with random crystallographic texture measured on ENGIN-X (red dots) and the simulated spectrum (black solid line). (b) Attenuation coefficient of an α-iron powder measured on ENGIN-X (red dots) and IMAT (blue squares) and the corresponding simulations (blue and red solid lines).
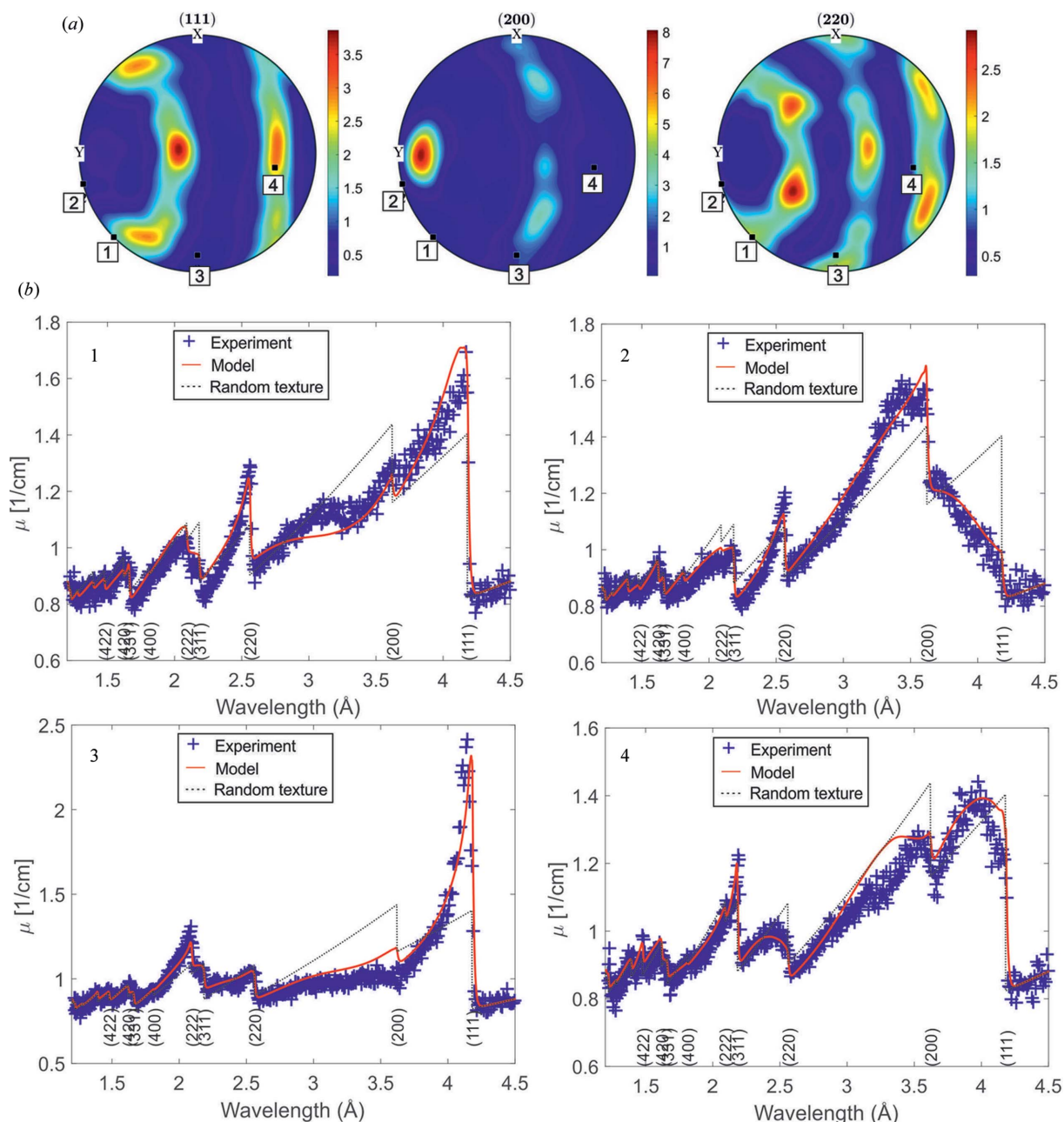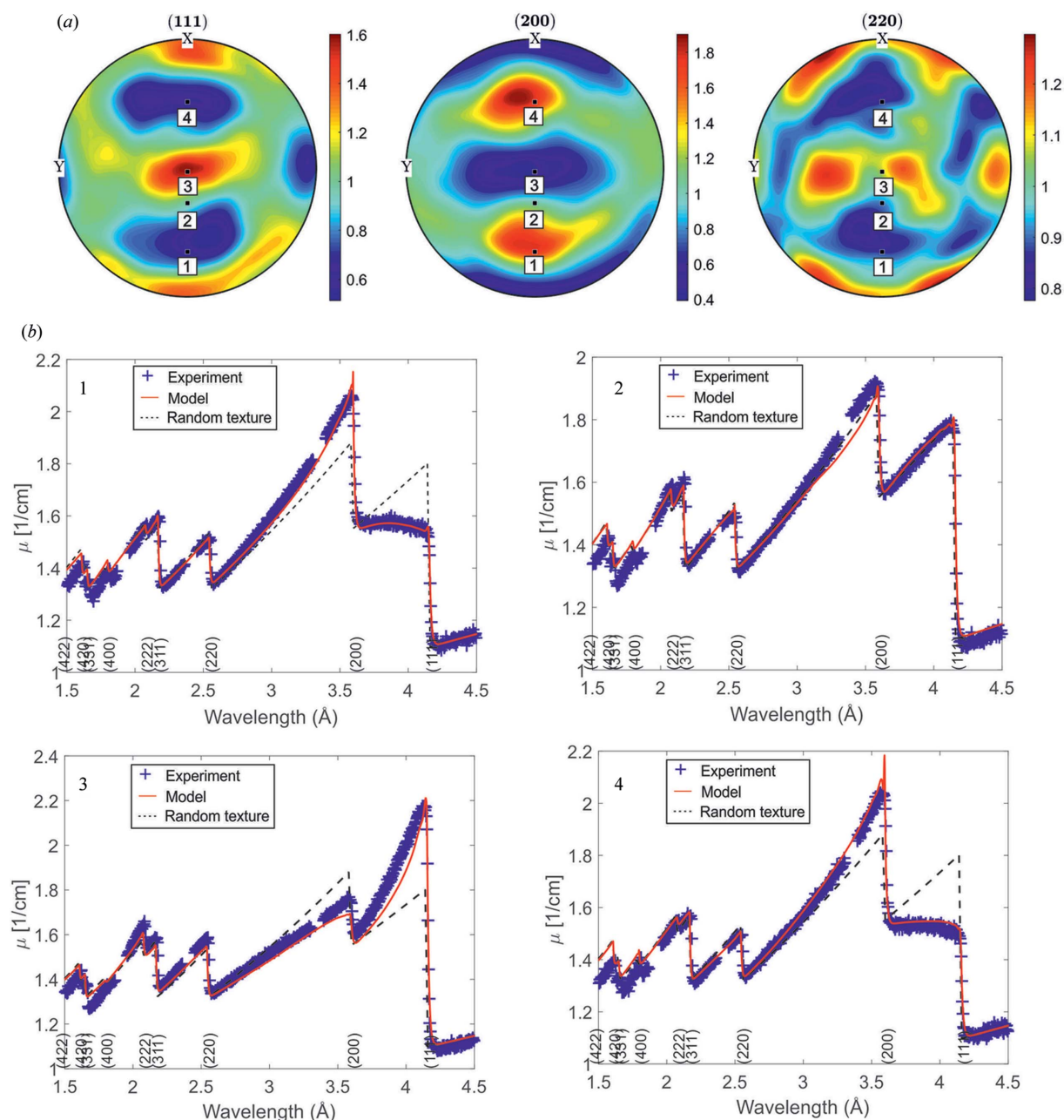
Figure 6
Results for the copper textured specimen. (*a*) Recalculated pole figures from the ODF produced from neutron diffraction experiments. (*b*) Experimental (blue crosses) and simulated (solid red lines) attenuation coefficients measured along the directions denoted 1 to 4 in the pole figures, and comparison with a random textured specimen (dotted black lines).

These values are mostly related to the minor differences observed for all orientations close to the (200) Bragg edge, where the sample displays the largest effects of preferred orientation.

7.3. Stainless steel laser powder-bed fusion sample

The model was also applied to a rectangular sample of 316L austenitic stainless steel produced by laser powder-bed fusion, which presents strong texture variation in the transverse direction, *i.e.* along *x* in Fig. 7 (Busi *et al.*, 2022). A tomography experiment was performed on RADEN at J-PARC (Japan),

rotating the sample with the rotation axis parallel to the LPBF build direction. A full description of the sample and experimental configuration employed during the measurement is given by Busi *et al.* (2022). The crystallographic texture of the sample was measured using conventional neutron diffraction on the GEM diffractometer (Kockelmann *et al.*, 2006). Fig. 7(*a*) shows the pole figures and the incident neutron beam direction in the sample reference system for four selected orientations, *i.e.* four different rotations around the building direction **Y**. In this case, within the model, the crystallographic texture was described by evaluating the volume fractions of the obtained ODF on an equi-spaced 5° resolution grid using

Figure 7
Results for the 316L LPBF specimen. (*a*) Recalculated pole figures from the ODF produced from neutron diffraction experiments where **Y** corresponds to the building direction. (*b*) Experimental (blue crosses) and simulated (solid red lines) attenuation coefficients measured along the directions denoted 1 to 4 in the pole figures, and comparison with a specimen with random texture (dashed black lines).

$\beta = 3.1°$, on top of a 0.1% volume fraction uniform portion to fulfil the normalization condition. The measured attenuation coefficients (blue crosses) and results of the simulations (solid red lines) for the selected beam orientations are shown in Fig. 7(*b*), together with the expected attenuation coefficient of a 316L sample with random crystallographic texture (dashed black lines). Again, good agreement is found between the model and the experimental data for all explored sample orientations, with R_p values of 4.1, 2.6, 4.8 and 4.3% for orientations 1 to 4, respectively. In particular, for orientations 1 and 4 the attenuation coefficient model has fully captured the symmetry of the crystallographic texture of the sample.

8. Discussion and conclusions

The presented model fully captures the complex dependence of the attenuation coefficient on the orientation distribution function and the specimen orientation, as demonstrated in Figs. 5, 6 and 7. In all cases, a very good overall agreement was found between the experimental data and simulations, with R_P around 10% or significantly lower. In contrast to *sinpol*, the model presented by Dessieux *et al.* (2018), where the discretization is performed in real space, here the FZ of the orientation space is discretized in regular grids with angularly very narrow components (unimodal components).
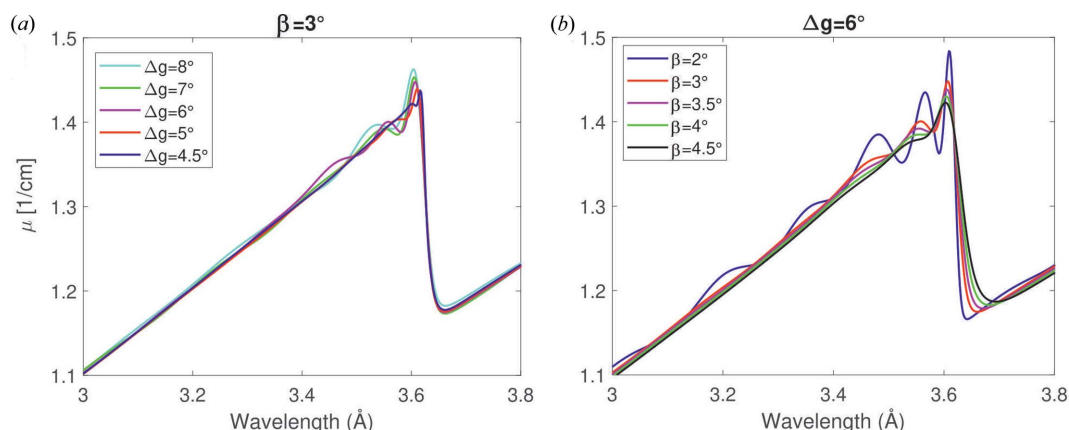
Figure 8
Simulated (200) Bragg edge of a randomly oriented copper specimen for (*a*) different equi-spaced grids with the same half-width $\beta = 3°$ and (*b*) different half widths with fixed grid resolution $\Delta g_i = 6°$.

This discretization allows optimization of the number of single-crystal orientations involved in the calculation, considering the instrument resolution and the statistical uncertainty of the experimental transmission spectra. This efficiently reduces the computation time required to perform a model fit by an order of magnitude [from 400 s using 10 000 individual orientations in *sinpol* (Dessieux *et al.*, 2018) to just 46 s using 9807 orientations in the current model] when using similar computers (2.50 GHz Intel Core i5 processor personal laptop). The reduced computation time of the proposed model opens the possibility of employing it for simulating more complex Bragg edge imaging experiments, *e.g.* spectral neutron tomography (Carminati *et al.*, 2020; Busi *et al.*, 2022) or time-resolved Bragg edge studies (Makowska *et al.*, 2015), without the need for computational clusters.

The proposed efficient discretization considers and is optimized to the instrumental performance, in particular the achievable resolution, which for a given experiment defines the required definition of the g_i grid centres and the β parameter of the unimodal distribution. Both parameters in the ODF decomposition (and in the resulting intensities and widths of Laue peaks) have a profound impact on the calculated spectra, as is shown in Fig. 8 for the (200) Bragg edge of a copper specimen with random crystallographic texture. Fig. 8(*a*) shows the impact of the resolution of the equi-spaced grid on the modelled Bragg edge shape (for a fixed half-width $\beta = 3°$), while Fig. 8(*b*) shows the effect of the half-width of the unimodal component for a fixed grid resolution $\Delta g_i = 6°$. This feature of being able to consider the instrumental capability, besides accelerating the fitting procedure significantly, facilitates superior fitting quality and results. The good agreement observed in Fig. 5 for both copper and iron powders measured on two imaging instruments with different resolutions is direct proof of the capability of the approach and model to describe the measured transmission spectra when the instrumentally determined parameters are properly defined. Similarly, Figs. 6 and 7 demonstrate the ability of the model to predict the attenuation spectra of textured materials, *i.e.* a textured copper sample and an additively manufactured 316L sample, measured in different orientations.

The instrumental resolution function adopted for the measurements performed at short-pulse spallation neutron sources is described by an asymmetric profile, which has been shown to be more suitable than a simple Gaussian function, as was implemented *e.g.* by Dessieux *et al.* (2019), for wavelength-resolved transmission experiments performed at such sources (Kropff *et al.*, 1982). The asymmetric profile allows a complete description of the specific Bragg edge tails observed on corresponding neutron imaging instruments, like those presented here, as can be appreciated from the difference curve shown at the bottom of Fig. 5(*b*). Moreover, the versatility of the proposed approach allows the implementation of different resolution functions by simply modifying the peak profile function, expanding the capabilities of the approach to model wavelength-resolved transmission measurements performed at different neutron sources and on particular instruments.

In summary, we have successfully and efficiently modelled the linear neutron attenuation coefficient spectra of textured polycrystalline materials, as demonstrated using a copper sample serving as a reference in texture studies of archaeological objects and a 316L stainless steel sample produced by laser powder-bed fusion additive manufacturing. In all cases, a very good overall agreement was found between the experimental data and the fits, validating the versatility of the model in predicting the attenuation coefficients of polycrystalline textured materials. This opens the possibility of including the proposed attenuation coefficient model, based on a parametric model of the ODF with a reduced number of texture components, into a least-squares fitting routine to refine the volume fractions of the selected components from wavelength-resolved neutron imaging experiments.

APPENDIX A
Bragg attenuation contribution of mosaic crystals

The spectrum $R(\lambda)$ of a mosaic crystal is described by a series of Laue peaks, characterized by their position λ_{hkl}, integrated area I_{hkl} and width ϖ_{hkl} (FWHM), resulting from all *hkl*

planes meeting the diffraction conditions within the wavelength range of the experiment,

$$R(\lambda) = \sum_{hkl} I_{hkl} P(\lambda_{hkl}, \varpi_{hkl}, \lambda). \qquad (18)$$

Here, the function $P(\lambda_{hkl}, \varpi_{hkl}, \lambda)$ describes the actual peak shape (with unit area), depending on the specific instrument. The peak position is given by the interplanar distance d_{hkl} and the angle α_{hkl} between the plane normal and the neutron beam,

$$\lambda_{hkl} = 2d_{hkl} \cos \alpha_{hkl}. \qquad (19)$$

The peak width ϖ_{hkl} is a function of the crystal mosaicity and mean-square microstrain within the sample, the instrument resolution, and the angle α_{hkl}. The integrated intensity I_{hkl} is a complex function of the structure factor of the plane, the mosaicity, the beam divergence, and the geometry, size and orientation of the specimen. The integrated intensity of the hkl peak is given, within the kinematic theory of diffraction, by $I_{hkl} = 1 - \exp(-l\mu_R^{hkl})$, where l is the crystal thickness in the neutron beam direction and μ_R^{hkl} is the integrated reflectivity of the hkl reflection (Zachariasen, 1945),

$$\mu_R^{hkl} = \frac{|F_{hkl}|^2 \lambda_{hkl}^4}{2v^2 \sin^2 \theta_{hkl}}. \qquad (20)$$

Here, $|F_{hkl}|$ is the structure factor (including the Debye–Waller factor), v is the volume of the unit cell and $\theta_{hkl} = \sin^{-1}(\lambda_{hkl}/2d_{hkl})$ is the Bragg angle for the reflection. In particular, for a thin specimen ($l \ll 1/\mu_R^{hkl}$) the integrated intensity becomes $I_{hkl} \simeq l\mu_R^{hkl}$. As a result, $R(\lambda)$ of an individual single crystal is written as

$$R(\lambda) = l \sum_{hkl} \mu_R^{hkl} P(\lambda_{hkl}, \varpi_{hkl}, \lambda). \qquad (21)$$

The peak profile function $P(\lambda_{hkl}, \varpi_{hkl}, \lambda)$ depends on the instrumental resolution function. For transmission experiments performed at pulsed sources, the neutrons are produced in short pulses and their wavelength is determined by their time of flight (TOF) along a fixed path between the moderator and the detector L,

$$\lambda = \frac{h}{mL}(t - t_0). \qquad (22)$$

h is Planck's constant, m the neutron mass and t_0 a delay time, representing the average time spent by the neutrons within the moderator and possible delays of the detection system. In such cases, the resolution function is defined by all the experimental errors contributing to the uncertainty in the arrival time of the neutron (t): the average time spent by the neutrons within the moderator (emission time t_e) and the time that the neutron employs travelling to the detector ($t_L = mL\lambda/h$). The instrumental resolution corresponds to the convolution of the probability distributions $P(t_e)$ and $P(t_L)$ associated with t_e and t_L, respectively. Here we adopt for the resolution function the model proposed by Kropff et al. (1982), consisting of a Gaussian of deviation $\upsilon_{hkl}(\lambda)$ convoluted with a truncated decaying exponential starting at t_0 and decaying with a time constant $\tau_{hkl}(\lambda)$. The decay constant $\tau_{hkl}(\lambda)$ is a characteristic property of the moderator, depending on its geometry and temperature, and its wavelength dependence can be obtained by measuring randomly oriented polycrystalline samples (Santisteban et al., 2001; Ramadhan et al., 2019). Employing this resolution function, the expression for a peak located at wavelength λ_{hkl} is

$$P(\lambda_{hkl}, [\tau_{hkl}, \upsilon_{hkl}], \lambda) = \frac{1}{\tau_{hkl}(\lambda)} \exp\left[-\frac{\lambda - \lambda_{hkl}}{\tau_{hkl}(\lambda)}\right]$$
$$\otimes \frac{1}{(2\pi)^{1/2} \upsilon_{hkl}(\lambda)} \exp\left[-\frac{(\lambda - \lambda_{hkl})^2}{2\upsilon_{hkl}(\lambda)^2}\right]$$
$$= \frac{1}{2\tau_{hkl}(\lambda)} \exp\left[-\frac{\lambda - \lambda_{hkl}}{\tau_{hkl}(\lambda)} + \frac{\upsilon_{hkl}(\lambda)^2}{2\tau_{hkl}(\lambda)^2}\right]$$
$$\times \mathrm{erfc}\left[-\frac{\lambda - \lambda_{hkl}}{2^{1/2}\upsilon_{hkl}(\lambda)} + \frac{\upsilon_{hkl}(\lambda)}{\tau_{hkl}(\lambda)}\right], \qquad (23)$$

where d_{hkl} is the interplanar distance for the (hkl) planes and α_{hkl} is the angle between the neutron beam and the normal to the reflecting crystal planes.

The FWHM of the peak shape of equation (23) does not have a simple analytical expression as a function of $\upsilon_{hkl}(\lambda)$, $\tau_{hkl}(\lambda)$ and λ_{hkl}, but it can be estimated for an hkl reflection by considering the uncertainties influencing the TOF arrival of the neutrons $t = t_e + mL\lambda/h$ as

$$\left(\frac{\Delta t}{t_{hkl}}\right)^2 = \left(\frac{\Delta t_e}{t_{hkl}}\right)^2 + \left(\frac{\Delta L}{L}\right)^2 + \left(\frac{\Delta \lambda_{hkl}}{\lambda_{hkl}}\right)^2, \qquad (24)$$

where Δt_e, ΔL and $\Delta \lambda_{hkl}$ are the uncertainties in the emission time, flight path and neutron wavelength, respectively. The relative uncertainty in the flight path is usually small $[(\Delta L/L) \simeq 10^{-5}]$ and can be neglected, while Δt_e is proportional to the decay constant $\tau_{hkl}(\lambda)$. The uncertainty in the neutron wavelength $\Delta \lambda_{hkl}$ comes from Bragg's law [equation (19)] and, assuming that there is no correlation between d_{hkl} and α_{hkl}, can be written as

$$\left(\frac{\Delta \lambda_{hkl}}{\lambda_{hkl}}\right)^2 = \left(\frac{\Delta d_{hkl}}{d_{hkl}}\right)^2 + (\Delta \alpha_{hkl})^2 \tan^2 \alpha_{hkl}, \qquad (25)$$

where $\overline{\varepsilon^2} = (\Delta d_{hkl}/d_{hkl})^2$ represents the mean-square elastic deformation of the crystal structure and $(\Delta \alpha_{hkl})^2$ comes from the finite distribution of scattering angles. $(\Delta \alpha_{hkl})^2$ depends on the divergence of the incident beam and the finite distribution of crystal orientations. Considering both contributions as Gaussian distributions with widths γ and β, respectively, $\upsilon_{hkl}(\lambda)$ can be written as

$$\upsilon_{hkl}(\lambda)^2 = \lambda_{hkl}^2 [\varepsilon^2 + (\gamma^2 + \beta^2) \tan^2 \alpha_{hkl}]. \qquad (26)$$

research papers

References

Artioli, G. (2007). *Appl. Phys. A*, **89**, 899–908.

Biswas, A., Vajragupta, N., Hielscher, R. & Hartmaier, A. (2020). *J. Appl. Cryst.* **53**, 178–187.

Bunge, H. J. (1982). *Texture Analysis in Materials Science: Mathematical Methods.* London: Butterworths.

Busi, M., Kalentics, N., Morgano, M., Griffiths, S., Tremsin, A. S., Shinohara, T., Logé, R., Leinenbach, C. & Strobl, M. (2021). *Additive Manuf.* **39**, 101848.

Busi, M., Polatidis, E., Malamud, F., Kockelmann, W., Morgano, M., Kaestner, A., Tremsin, A., Kalentics, N., Logé, R., Leinenbach, C., Shinohara, T. & Strobl, M. (2022). *Phys. Rev. Mater.* **6**, 053602.

Carminati, C., Strobl, M., Minniti, T., Boillat, P., Hovind, J., Morgano, M., Holm Rod, T., Polatidis, E., Valsecchi, J., Mannes, D., Kockelmann, W. & Kaestner, A. (2020). *J. Appl. Cryst.* **53**, 188–196.

Dessieux, L. L., Stoica, A. D. & Bingham, P. R. (2018). *Rev. Sci. Instrum.* **89**, 025103.

Dessieux, L. L., Stoica, A. D., Bingham, P. R., An, K., Frost, M. J. & Bilheux, H. Z. (2019). *Nucl. Instrum. Methods Phys. Res. B*, **459**, 166–178.

Fermi, E., Sturm, W. J. & Sachs, R. G. (1947). *Phys. Rev.* **71**, 589–594.

Granada, J. R. (1984). *Z. Naturforsch.* **39**, 1160–1167.

Hielscher, R. (2013). *J. Multivariate Anal.* **119**, 119–143.

Hielscher, R. & Schaeben, H. (2008). *J. Appl. Cryst.* **41**, 1024–1037.

Jansen, E., Schäfer, W. & Will, G. (1994). *J. Appl. Cryst.* **27**, 492–496.

Kardjilov, N., Manke, I., Hilger, A., Williams, S., Strobl, M., Woracek, R., Boin, M., Lehmann, E., Penumadu, D. & Banhart, J. (2012). *Int. J. Mater. Res.* **103**, 151–154.

Kockelmann, W., Chapon, L. C. & Radaelli, P. G. (2006). *Physica B*, **385–386**, 639–643.

Kockelmann, W., Zhang, S. Y., Kelleher, J. F., Nightingale, J. B., Burca, G. & James, J. A. (2013). *Phys. Procedia*, **43**, 100–110.

Kocks, U. F. (2000). *Texture and Anisotropy: Preferred Orientations in Polycrystals and Their Effect on Materials Properties.* Cambridge University Press.

Kropff, F., Granada, J. R. & Mayer, R. E. (1982). *Nucl. Instrum. Methods Phys. Res.* **198**, 515–521.

Laliena, V., Vicente-Álvarez, M. Á. & Campo, J. (2020). *J. Appl. Cryst.* **53**, 512–529.

Lehmann, E. H., Frei, G., Vontobel, P., Josic, L., Kardjilov, N., Hilger, A., Kockelmann, W. & Steuwer, A. (2009). *Nucl. Instrum. Methods Phys. Res. A*, **603**, 429–438.

Lehmann, E. H., Peetermans, S., Josic, L., Leber, H. & van Swygenhoven, H. (2014). *Nucl. Instrum. Methods Phys. Res. A*, **735**, 102–109.

Makowska, M. G., Strobl, M., Lauridsen, E. M., Frandsen, H. L., Tremsin, A. S., Kardjilov, N., Manke, I., Kelleher, J. F. & Theil Kuhn, L. (2015). *J. Appl. Cryst.* **48**, 401–408.

Malamud, F. (2016). PhD thesis, Instituto Balseiro, Rio Negro, Argentina.

Malamud, F. & Santisteban, J. R. (2016). *J. Appl. Cryst.* **49**, 348–365.

Malamud, F., Santisteban, J. R., Gao, Y., Shinohara, T., Oikawa, K. & Tremsin, A. (2022). *J. Appl. Cryst.* **55**, 228–239.

Malamud, F., Santisteban, J. R., Vicente Alvarez, M. A., Bolmaro, R., Kelleher, J., Kabra, S. & Kockelmann, W. (2014). *J. Appl. Cryst.* **47**, 1337–1354.

Morgano, M., Kalentics, N., Carminati, C., Capek, J., Makowska, M., Woracek, R., Maimaitiyili, T., Shinohara, T., Loge, R. & Strobl, M. (2020). *Additive Manuf.* **34**, 101201.

Ramadhan, R. S., Kockelmann, W., Minniti, T., Chen, B., Parfitt, D., Fitzpatrick, M. E. & Tremsin, A. S. (2019). *J. Appl. Cryst.* **52**, 351–368.

Santisteban, J. R. (2005). *J. Appl. Cryst.* **38**, 934–944.

Santisteban, J. R., Daymond, M. R., James, J. A. & Edwards, L. (2006). *J. Appl. Cryst.* **39**, 812–825.

Santisteban, J. R., Edwards, L. & Stelmukh, V. (2006). *Physica B*, **385–386**, 636–638.

Santisteban, J. R., Edwards, L., Steuwer, A. & Withers, P. J. (2001). *J. Appl. Cryst.* **34**, 289–297.

Santisteban, J. R., Vicente-Alvarez, M. A., Vizcaino, P., Banchik, A. D., Vogel, S. C., Tremsin, A. S., Vallerga, J. V., McPhate, J. B., Lehmann, E. & Kockelmann, W. (2012). *J. Nucl. Mater.* **425**, 218–227.

Sato, H. (2017). *J. Imaging*, **4**, 7.

Sato, H., Kamiyama, T., Iwase, K., Ishigaki, T. & Kiyanagi, Y. (2011). *Nucl. Instrum. Methods Phys. Res. A*, **651**, 216–220.

Sato, H., Takada, O., Iwase, K., Kamiyama, T. & Kiyanagi, Y. (2010). *J. Phys. Conf. Ser.* **251**, 012070.

Schaeben, H. (1997). *Phys. Status Solidi B*, **200**, 367–376.

Schneider, J. R. (1974). *J. Appl. Cryst.* **7**, 541–546.

Sears, V. F. (1997). *Acta Cryst.* A**53**, 35–45.

Sears, V. F. & Shelley, S. A. (1991). *Acta Cryst.* A**47**, 441–446.

Shinohara, T., Kai, T., Oikawa, K., Nakatani, T., Segawa, M., Hiroi, K., Su, Y., Ooi, M., Harada, M., Iikura, H., Hayashida, H., Parker, J. D., Matsumoto, Y., Kamiyama, T., Sato, H. & Kiyanagi, Y. (2020). *Rev. Sci. Instrum.* **91**, 043302.

Shiota, Y., Hasemi, H. & Kiyanagi, Y. (2017). *Phys. Procedia*, **88**, 128–133.

Vicente Alvarez, M. A., Laliena, V., Malamud, F., Campo, J. & Santisteban, J. (2021). *J. Appl. Cryst.* **54**, 903–913.

Vogel, S. (2000). Dissertation, Christian-Albrechts-Universität zu Kiel, Germany. https://macau.uni-kiel.de/receive/diss_mods_00000330.

Zachariasen, W. H. (1945). *Theory of X-ray Diffraction in Crystals.* Chichester: John Wiley & Sons.